EUROFUSION WPJET4-PR(16) 14882

M Nocente et al.

A generalized Abel inversion method for gamma-ray imaging of thermonuclear plasmas

Preprint of Paper to be submitted for publication in
Journal of Instrumentation

This work has been carried out within the framework of the EUROfusion Consortium and has received funding from the Euratom research and training programme 2014-2018 under grant agreement No 633053. The views and opinions expressed herein do not necessarily reflect those of the European Commission.

Prepared for submission to JINST

1ST[TH] Workshop on "Imaging"
7th-10th September 2015
Varenna, Italy

A generalized Abel inversion method for gamma-ray imaging of thermonuclear plasmas

M. Nocente,[a,b,c,1] **A. Pavone,**[a,b] **M. Tardocchi,**[a,c] **V. Goloborod'ko,**[a,d] **K. Schoepf,**[a,d] **V. Yavorskij**[a,d,e] **and JET Contributors**[2]

[a] *EUROfusion Consortium, JET, Culham Science Centre, Abingdon, OX14 3DB, UK*
[b] *Dipartimento di Fisica "G. Occhialini", Universita' di Milano-Bicocca, Milano, Italy*
[c] *Istituto di Fisica del Plasma "P. Caldirola", Consiglio Nazionale delle Ricerche Milano, Italy*
[d] *Institute for Theoretical Physics, University of Innsbruck Innsbruck, Austria*
[e] *Institute for Nuclear Research, Ukrainian Academy of Sciences Kiev, Ukraine*

E-mail: massimo.nocente@mib.infn.it

Abstract: A method to determine the gamma-ray emissivity profile from measurements along a few multiple collimated lines of sight in thermonuclear plasmas is presented. The algorithm is based on a generalisation of the known Abel inversion and takes into account the non circular shape of the plasma flux surfaces and the limited number of data points available. The method is applied to synthetic experimental measurements originating from parabolic and non parabolic JET gamma-ray emissivity profiles, where the aim is to compare the results of the inversion with the original, known input parameters. We find that profile parameters, such as the peak value, width and centre of the emissivity, are determined with an accuracy between 1 and 20% for parabolic and 2 to 25% for non parabolic profiles, respectively, which compare to an error at the 10% level for the input data. The results presented in this paper are primarily of relevance for the reconstruction of emissivity profiles from radiation measurements in tokamaks, but the method can also be applied to measurements along a sparse set of collimated lines of sight in general applications, provided that the surfaces at constant emissivity are known to have rotational simmetry.

Keywords: Nuclear instruments and methods for hot plasma diagnostics; Plasma diagnostics - interferometry, spectroscopy and imaging

[1] Corresponding author.

[2] See the Appendix of F. Romanelli et al., Proceedings of the 25th IAEA Fusion Energy Conference 2014, Saint Petersburg, Russia

Contents

1 Introduction

Gamma-ray measurements play a fundamental role for the investigation of fast ion physics in high performance fusion plasmas [1–3]. Gamma-ray emission can arise from a variety of nuclear reactions either between supra-thermal ions and plasma impurities resulting from erosion of the tokamak first wall (^{12}C and ^{9}Be at the Joint European Torus (JET)[4–7]), or due to one step processes in which two light ions merge into a heavier one and release their excess energy by emission of a gamma-ray [6, 8]. From the experimental point of view, efforts have mostly been put in the development of high resolution detectors, such as based on High Purity Germanium (HpGe), and that were used to unambiguously measure the kinematic broadening of characteristic gamma-ray emission peaks [9], in order to determine parameters of the energy distribution function of the fast ions responsible for the emission [10]. More recently, neutron hard detectors based on the $LaBr_3$ crystal [11–15] have been developed for applications at the MHz counting rates [16] expected from forthcoming JET deuterium-tritium plasmas, for which HpGe detectors cannot be used.
All of the above developments were motivated by the need to determine the energy distribution of the fast ions and thus focused on optimizing energy resolution for a detector on a single collimated line of sight (LOS). Another important quantity to measure is however the spatial profile of the emission, which requires the simultaneous detection of gamma-ray radiation along multiple LOSes and the use of suitable algorithms to determine the image of gamma-ray emission from a set of measurements along thin chords. At JET, for example, a system based on multiple chord measurements (called camera) exists and has been traditionally used to reconstruct the neutron emission profile. More recently it has been also used for gamma-ray imaging [2], albeit with CsI detectors having an insufficient energy resolution to distinguish characteristic gamma-ray peaks and limited to counting rates of few kHz, which makes images obtained so far rather uncertain. In order to overcome these limitations, an upgrade is presently ongoing and aims at combining good energy resolution, high rate capability and compact dimensions for the detectors in view of enabling high resolution gamma-ray imaging in full performance, forthcoming JET deuterium-tritium plasmas [17, 18].
Motivated by the upgrade of the JET gamma-ray camera and the resulting future availability of high

quality data, in this paper we present a new algorithm that could be used for the reconstruction of the image of gamma-ray emission from multiple collimated measurements at JET and based on a generalization of the Abel method for an infinite set of thin, parallel LOSes [19]. Our aim is here to provide a fast algorithm that may be useful to evaluate the gamma-ray emission profile in between high power discharges with reasonable accuracy, so to extract information that can be used for a rapid assessment of the main outcomes of a particular plasma scenario. This can be of help to determine the gross features of the emission, before a detailed (but time consuming) analysis based on first principle modelling of the fast ion energy distribution and on forward fitting of the data is performed at a later stage [20].
The paper is organised as follows. In section 2, after a brief description of the JET camera systems and their peculiarities, we present the mathematics that stands at the basis of our algorithm. In sections 3 and 4 the method is demonstrated for parabolic and non-parabolic profiles using synthetic experimental data as input and for which the initial profile solution is known. In this way, we can compare the outcome of the inversion with the starting emission profile and assess the precision on the reconstructed profile provided by our method. Conclusions are finally presented in section 5.

2 Generalized Abel inversion method for the JET gamma-ray camera

The JET tokamak is presently equipped with two systems of multiple lines of sights, called with the word "cameras" and illustrated in figure 1.

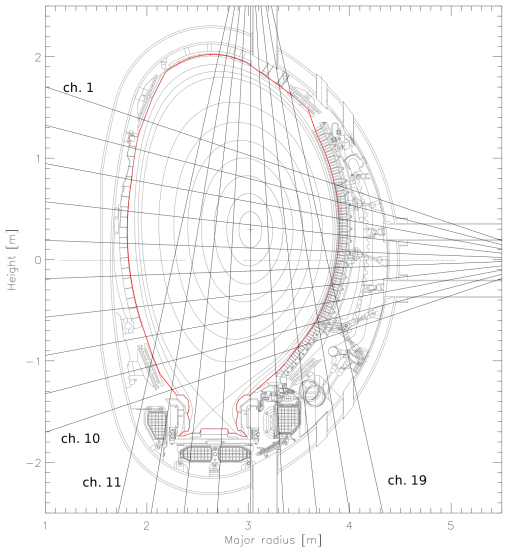

Figure 1. Schematics of the two JET gamma-ray cameras (vertical and horizontal) with illustrations of their 19 lines of sight. Channels 1 to 10 belong to the horizontal camera. Channels 11 to 19 belong to the vertical camera. The elliptic line in the figure represent the plasma flux surfaces.

The horizontal camera consists of 10 lines of sight that cross the plasma cross section (poloidal plane) horizontally; the vertical camera is made of 11 lines of sight that view the plasma vertically. The lines of sight are fan shaped and are further arranged so to provide a better coverage of the plasma core, where most of gamma-ray emission is expected to come from. As the practical

implementation of a camera system in a tokamak environment requires massive concrete shielding for collimation purposes, only a limited number of lines of sight can typically be implemented, which results in rather poor spatial resolution of the measurements. For example, in the case of the JET system, the horizontal camera views the plasma core from z=1.0 m to z=-1.0 m and thus provides a spatial resolution in the vertical direction of about 20 cm. Similarly, the vertical camera covers the radial core region roughly between R=2.5 and 4 m, with a resolution in the radial direction of the order of 15 cm. R and z are here the radial and vertical coordinates of the poloidal plane. Due to the fan shaped arrangement of the channels, we also note that there is a highly non homogeneous coverage of the profile along the poloidal angle θ. All of the channels give measurements at $\theta \approx 0°$(horizontal camera) and $\theta \approx 90°$(vertical camera) and there is no information on the profile for angles in between. Thus, a direct inversion of the JET camera data is a very ill-posed problem and prone to the generation of artefacts unless information from other diagnostic systems is embedded in the reconstruction method. Besides, angular information resulting from a full two dimensional (R,θ) inverted profile may be questionable.

As the angular limitation is difficult to overcome, unlike previous methods [21–23], we propose a way to determine only the radial profile of the emission, under the assumption that the shape of the surfaces corresponding to constant gamma-ray emissivity are known and coincide with the magnetic flux surfaces. These are the solution of the so called Grad-Shafranov equation and are generally known with good accuracy from magnetic measurements[24]. In this sense, our algorithm is a generalisation of the known Abel inversion, which was developed for circular surfaces of constant emission [19]. The mathematical derivation of the method is as follows.

In geometrical terms, and with reference to figure 2, each line of sight can be described by two parameters, a radial coordinate s and an angle ϕ.

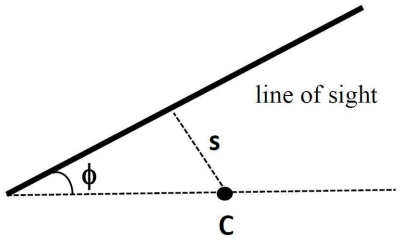

Figure 2. A collimated line of sight is described by two parameters. a) A radial coordinate s, defining the distance of the line of sight with respect to the center of the concentric surfaces of constant emission b) an angle ϕ associated to the inclination of the chord with respect to the horizontal direction.

In the following, we shall further adopt the notation of [25] and use $y_\gamma(s)$ to denote the local gamma-ray emissivity. This will be a function of a radial coordinate s in the poloidal plane and gives the number of gamma-rays/second/cm^3 born at each plasma position. For narrow, well collimated lines of sight, such as those of the JET cameras, the gamma-ray flux (also called brightness b_λ) measured by the detector at the end of a specific channel and along the corresponding chord $\lambda(s,\phi)$ is related to the emissivity by the line integral

$$b_\lambda(s,\phi) = \int_{\lambda(s,\phi)} y_\gamma(l)dl \tag{2.1}$$

where dl is an infinitesimal segment along the chord $\lambda(s, \phi)$. With the word "inversion" we mean to determine $y_\gamma(s)$ given a measured b_λ for each chord of the JET gamma-ray cameras.
The Abel method provides an answer to the inversion problem when $y_\gamma(s)$ has circular symmetry and if the brightness is measured along an infinite set of parallel lines of sight at increasing distance from the origin, i.e. if $s = 0 \ldots + \infty$ and $\phi = 0$ in equation 2.1. In this case

$$y_\gamma(s) = -\frac{1}{\pi} \int_s^{+\infty} \frac{db(s', 0)}{ds'} \frac{ds'}{\sqrt{s'^2 - s^2}} \tag{2.2}$$

In order to generalize such a method for tokamak plasmas, we can proceed in the following way. In the first place, since the flux surfaces are in general not circular, we interpret the s coordinate as the normalised poloidal radius which identifies each flux surface[24]. This is defined as

$$s = \sqrt{\frac{\psi}{\psi_{\mathrm{LCFS}}}} \tag{2.3}$$

where ψ is the poloidal flux function and LCFS denotes the last closed flux surface.
In the second place, as there is only a limited number of chords available, equation 2.1 needs to be discretised in a suitable way. With reference to figure 3, for each chord of the JET gamma-ray there is only one flux surface that is tangent to it. Therefore, the poloidal plane can be divided in 19 concentric regions bounded by the flux surfaces tangent to the 19 camera chords and the LCFS.

The region between two concentric surfaces defines a pixel of the inversion problem. As starting guess of the inversion, we assume that the emissivity y is constant in each pixel so that equation 2.1 is recast as

$$\boldsymbol{b} = L\boldsymbol{y} \tag{2.4}$$

Here $\boldsymbol{b}$ is a column array containing the 19 brightness values associated to each channel of the JET camera and $\boldsymbol{y}$ is the column array of the emissivities in each of the 19 pixels. The element L_{ij} of the L matrix is the length of the i-th chord inside the j-th pixel. The L matrix is fully known, as it can be evaluated from the geometrical arrangement of the lines of sight and the known flux surfaces. In principle, we could already obtain y from direct inversion of equation 2.4, i.e.

$$\boldsymbol{y} = L^{-1}\boldsymbol{b} \tag{2.5}$$

In practical applications, however, this yields an extremely irregular solution for the following reasons. On one hand, the real gamma-ray emissivity $y(s)$ is not constant inside each of the pixels implied by figure 3 and as surmised in the derivation of 2.4. Moreover, brightness measurements are typically subject to systematic as well as statistical errors up to the 10% level, which are significantly amplified by the inversion, unless proper smoothing is applied.
Let us consider instead a virtual set of vertical chords C_i that are tangent to the same pixels. For each flux surface of figure 3, there are two of such vertical LOSes, one to the left C_i^L and one to the right C_i^R. Similarly to equation 2.4, we can write an inversion equation for the virtual vertical chords to the left and to the right of the flux surfaces, i.e.

$$\boldsymbol{b}_{\boldsymbol{L}}^{\boldsymbol{V}} = V^L\boldsymbol{y} \tag{2.6}$$

and

$$\boldsymbol{b}_{\boldsymbol{R}}^{\boldsymbol{V}} = V^R\boldsymbol{y} \tag{2.7}$$

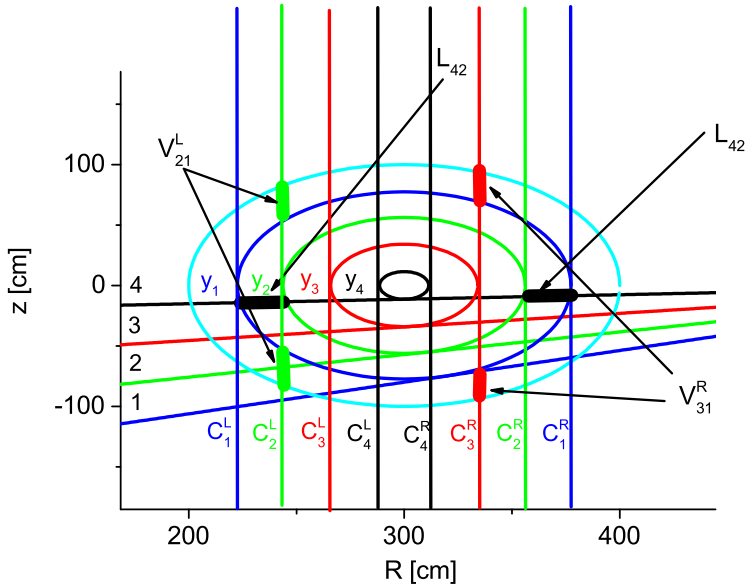

Figure 3. Geometrical representation of the pixel structure induced by the 19 JET lines of sight in the inversion problem. Each chord i of the JET gamma-ray camera identifies a flux surface that is tangent to it. The area between two tangent flux surfaces is a pixel at constant emissivity y_i. L_{ij} is the length of chord i inside pixel j. Each flux surface i also identifies a set of tangent virtual vertical chords, to the left (denoted with C_i^L) and to the right (C_i^R). The length of the virtual vertical chord i inside pixel j is indicated with V_{ij}^L (left chord) and V_{ij}^R (right chord). Only 4 lines of sight are shown for simplicity.

where $\boldsymbol{b_L^V}$, $\boldsymbol{b_R^V}$ are the arrays of the brightnesses associated to the virtual vertical chords to the left/right and the i, j element of V^L, V^R is the length of C_i^L,C_i^R inside the j-th pixel. $\boldsymbol{b_{R,L}^V}$ are not known but can be calculated from combination of 2.4, 2.6 and 2.7, i.e.

$$\boldsymbol{b_{L,R}^V} = V^{L,R} L^{-1} \boldsymbol{b} \tag{2.8}$$

If the hypothesis that constancy of gamma-ray emission on the flux surfaces is correct, the $\boldsymbol{b_{L,R}^V}$ data should lie on one curve. Deviations can arise due to errors in the experimental brightness $\boldsymbol{b}$, as well as uncertainties in the reconstruction of the flux surfaces obtained from the solution of the Grad-Shafranov equation starting from magnetic measurements. The $\boldsymbol{b_{L,R}^V}$ values can however be fitted to find a smooth function $\boldsymbol{b}(s)$ for $s < 0$ (left values) and $s > 0$ (right values), respectively. From $\boldsymbol{b}(s)$ we finally obtain $\boldsymbol{y}(s)$ by direct inversion of equations 2.6 and 2.7, i.e.

$$\boldsymbol{y}(s) = V^{-1L} \boldsymbol{b}(s) \; s > 0 \tag{2.9}$$

and

$$\boldsymbol{y}(s) = V^{-1R} \boldsymbol{b}(s) \; s < 0 \tag{2.10}$$

The full inversion procedure described here has been implemented in a python script running on the JET Analysis Cluster and takes about 1-2 minutes of computational time for a full inversion,

with some further time (say, 10 minutes) required by the operator to determine the fit parameters of the vertical projections. In the following sections we demonstrate the method for parabolic and non-parabolic emissivity profiles.

3 Inversion of parabolic emissivity profiles

The neutron and gamma-ray emissivities from JET plasmas have often been described in terms of a generalised parabola, i.e.

$$y(s) = y_0 \cdot (1 - s^2)^\nu \tag{3.1}$$

where y_0 is the peak emissivity, typically occurring on the magnetic axis, and ν is the peaking factor. The latter is related to the half width w of the profile by [25]

$$\nu = -\frac{\ln 2}{\ln (1 - w^2)} \tag{3.2}$$

Typical values for w are in the range $0.15 < w < 0.6$ at JET. A parabolic parametrization of the emissivity is valid for most plasmas, either with ohmic heating or with on axis neutral beam injection (NBI) or radio frequency heating, but for the case of strong off-axis NBI (see the next paragraph). As a test of our algorithm we can thus investigate its capability to determine the y_0 and w parameters of the emissivity profile, starting from synthetic brightness data for each channel of the JET cameras.

Figure 4 shows the gamma-ray emissivity in the poloidal plane when $y_0 = 8 \cdot 10^7$ cm^{-3}s^{-1} and $w = 0.3$. The magnetic equilibrium obtained in JET discharge 40214 at t=6.7s was used for the flux surfaces and to calculate the s coordinate. The lines of sight of the JET cameras are represented by dashed lines in the figure. Most of the emissivity is concentrated in a rather localised region of the poloidal cross section, say between R=250 cm to 350 cm and z=-50 cm to 100 cm. Outside this region, the emissivity drops by more than 10 times with respect to its peak value y_0. We therefore note that only 5 vertical and 6 horizontal channels observe the core region of y. This suggests the fact that, in practical applications, the emissivity profile is often reconstructed from a sparser dataset than the one implied by the 19 channels.

Figure 5 illustrates synthetic brightness values for each channel of the JET cameras and for the emissivity profile described above. In order to obtain these data, we have evaluated equation 2.1 and added a Gaussian noise at the 10% level to the results, so to mimic the effect of the typical experimental uncertainties. Data in figure 5 are the starting point of the inversion problem.

Following the procedure described in section 2, as a first step of the inversion, equations 2.6 and 2.7 were used to project the synthetic experimental data on the virtual vertical chords, with the results shown in figure 6 left.

Apart from some scatter due to noise in the original data, the projected brightnesses lie on a regular curve and a clear symmetry is observed between points at $s > 0$ and $s < 0$. Some additional scatter is observed for points close to the magnetic axis ($s \approx 0$), which may be due to additional uncertainties in the reconstruction of the innermost flux surfaces. A fit with a parabolic function was separately performed for the left and right projected brightnesses so to obtain a smooth function $\boldsymbol{b}(s)$. The inversion of $\boldsymbol{b}(s)$ with equations 2.9 and 2.10 is shown in figure 6 right. Here we note

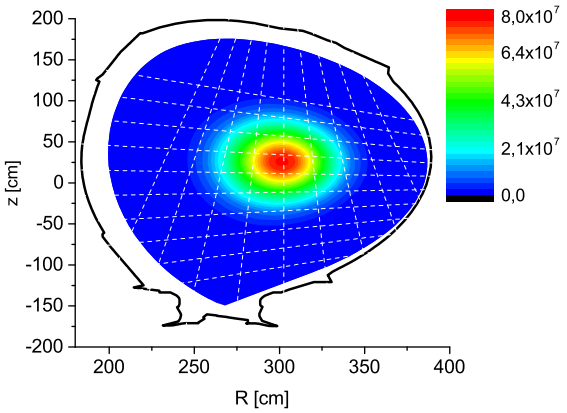

Figure 4. Gamma-ray emissivity in the poloidal plane for the case of a parabolic profile with $y_0 = 8 \cdot 10^7$ cm^{-3}s^{-1} and $w = 0.3$. Units for the emissivity are cm^{-3}s^{-1}. The dashed lines show the 19 channels of the JET cameras. The black line is the tokamak first wall.

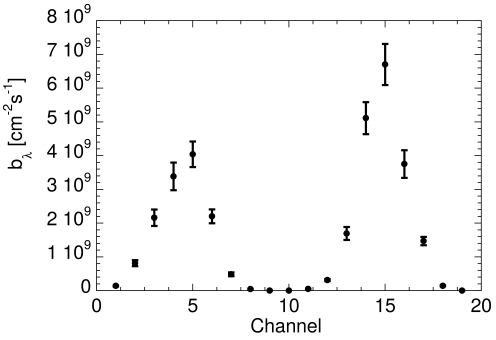

Figure 5. Experimental synthetic brightnesses for each channel of the JET cameras when the emissivity is that shown in figure 4. A Gaussian noise at the 10% level has been added.

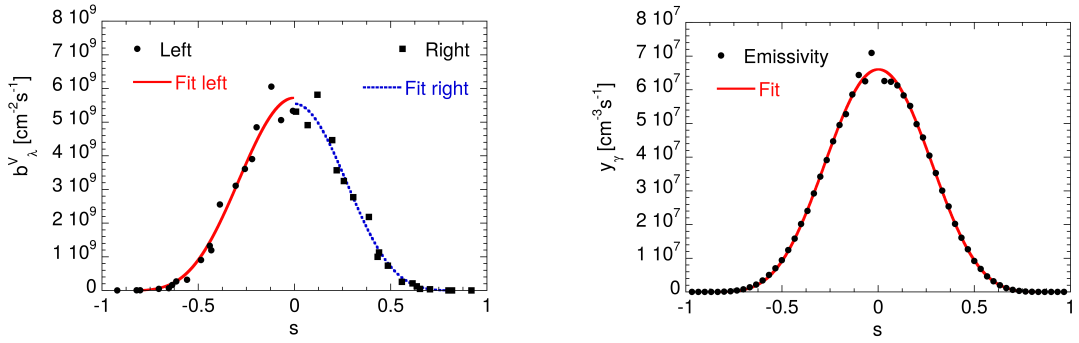

Figure 6. (left) Projection of the synthetic experimental brightness of figure 5 on a set of virtual vertical lines of sight for $s > 0$ and $s < 0$. Each projection is separately fitted with a parabolic function (solid and dashed lines). (right) Inverted emissivity profile obtained by applying equations 2.9 and 2.10 to each of the two fits of the left figure. The solid line is a parabolic fit of the inverted emissivity.

that the inverted data lie very well on a parabola, but for the data points around $s = 0$, which show some slight deviations, probably still due to uncertainties associated to the innermost flux surfaces. In order to compare the width and peak value of the inverted data in figure 6 with those expected, we have performed a parabolic fit with equation 3.1, where w and y_0 were left as free parameters. The results are $y_0 = 6.6 \cdot 10^7 \mathrm{cm}^{-3}\mathrm{s}^{-1}$ and $w = 0.311$, which deviate by 17% and 4% only from the expected values ($y_0 = 8 \cdot 10^7 \mathrm{cm}^{-3}\mathrm{s}^{-1}$ and $w = 0.3$).
A similar analysis procedure was repeated for parabolic profiles with different widths in the range $0.15 < w < 0.6$. Table 1 summarises some of the results obtained. In all cases, our algorithm was able to determine the width and peak values of the profile with an error between 5% and 20%. From the table we also observe that deviations from the expected values are in general smaller for wider profile widths, as a larger number of chords provides non null data in these cases. Comparable results were finally obtained when the centre of the emissivity profile had a shift with respect to the magnetic axis at $s = 0$, thus demonstrating the robustness of our algorithm. In all cases, we conclude that, for parabolic profiles, our algorithm can reliably determine the peak and width of the emissivity with an uncertainty in the range between 5 to 20%, which is sufficient in practical applications.

Table 1. Comparison between inversion results and expected values for the width w and peak y_0 in case of parabolic emissivity profiles described by equation 3.1. Results are reported for 3 different profile widths, $w = 0.15, 0.45, 0.6$

y_0 [$\mathrm{cm}^{-3}\mathrm{s}^{-1}$]			w		
Expected	Inversion result	Difference (%)	Expected	Inversion result	Difference (%)
$8.00 \cdot 10^7$	$6.56 \cdot 10^7$	18	0.15	0.16	6.7
$8.00 \cdot 10^7$	$7.96 \cdot 10^7$	0.5	0.45	0.43	3.8
$8.00 \cdot 10^7$	$7.97 \cdot 10^7$	0.4	0.6	0.58	3.3

4 Inversion of non parabolic emissivity profiles

A significantly more challenging inversion problem is provided by non parabolic profiles. These can result from off axis NBI heating and are not parametrised by means of simple analytical formulas. In order to evaluate the gamma-ray emissivity profile that may be expected from a high power JET deuterium-tritium plasma with off axis heating, we have considered a detailed simulation of gamma-ray emission from the $^9\mathrm{Be}(\alpha, \mathrm{n}\gamma)^{12}\mathrm{C}$ reaction [5] in which the α particle distribution function was the result of a calculation with the FIDIT code [26, 27]. In the FIDIT calculation, the plasma was divided into 220 cells and a slowing down α particle distribution was evaluated for each of the cells. Plasma parameters from JET high performance deuterium discharge 40214 with off-axis heating were used, but for a presumed 50:50 deuterium-tritium plasma composition. A constant $^9\mathrm{Be}$ concentration at the 1% level was further adopted. The calculation of the corresponding gamma-ray emissivity from $^9\mathrm{Be}(\alpha, \mathrm{n}\gamma)^{12}\mathrm{C}$ was based on the GENESIS Monte Carlo code [9, 28].
Figure 7 top shows the alpha particle density evaluated by FIDIT with the corresponding gamma-ray emissivity on the bottom.

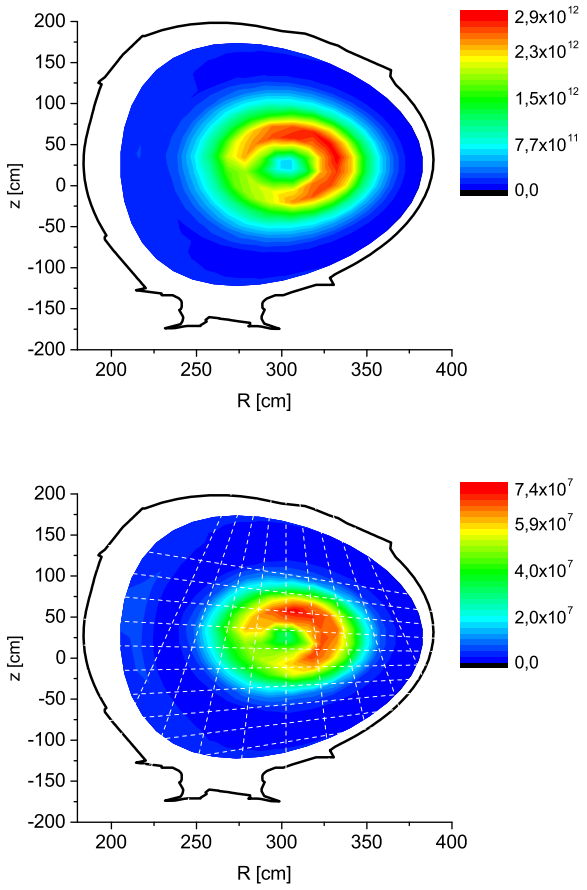

Figure 7. (top) FIDIT calculation of the α particle density (cm^{-3})in JET discharge 40214 with a presumed 50:50 deuterium-tritium composition (bottom) Calculated gamma-ray emissivity from the $^{9}Be(\alpha, n\gamma)^{12}C$ reaction evaluated for the same discharge. The dashed lines show the 19 channels of the JET cameras. The black line is the tokamak first wall. Units for the emissivity are $cm^{-3}s^{-1}$.

By comparing the two figures, we clearly note that there is qualitatively a high similarity between the two profiles so that a measurement of the gamma-ray emissivity profile provides information on the corresponding slowing down α particle spatial distribution in the plasma. Here we however do not discuss the detailed relation between the two figures, but we rather take figure 7 bottom as the image we would like to reconstruct from the 19 synthetic experimental brightnesses presented in figure 8 and evaluated with equation 2.1. A Gaussian noise at the 10% level was added also in this case when evaluating data in figure 8, similarly to the parabolic profiles presented in section 3.

The main challenge associated to non parabolic profiles is that the emissivity has variations in the poloidal direction, so that the profile is inherently two dimensional and in principle not suitable for the generalised Abel inversion algorithm of section 2. We also note that, even if a 2-dimensional algorithm such as those in references [21–23] were to be adopted, there would still be a high degree of uncertainty associated to the poloidal reconstruction of the profile, given the limited angular

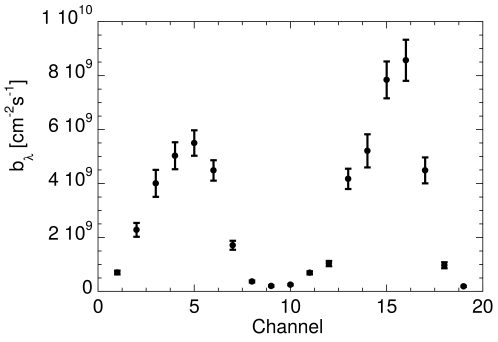

Figure 8. Synthetic experimental brightness values corresponding to the emissivity profile in figure 7 bottom. A Gaussian noise at the 10% level has been added.

coverage of the JET camera LOSes.

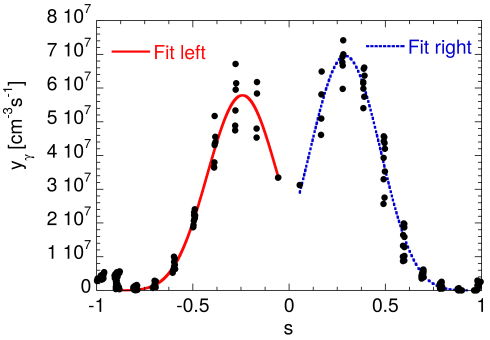

Figure 9. Radial projection of the gamma-ray emissivity profile in figure 7 bottom. A fit with a parabolic function (equation 3.1) was separately performed for data at $s < 0$ and $s > 0$ and is shown by solid and dashed lines in the figure.

On the other hand, we can consider a projection of the profile along the radial coordinate (figure 9) and observe that, although there is some scattering due to poloidal variations of the profile at each given s position, data can still be fitted by means of two parabolas, one for $s < 0$ and the other for $s > 0$. The centre of both parabolas now occurs at a position $s = s_C$, where $s_C \neq 0$. The aim of the generalised Abel inversion can be thus set to determine the peak y_0, width w and centre s_C of each of the two parabolas describing the radial projection of the emissivity profile.
The same steps involved in the inversion of brightness data for parabolic profiles were followed starting from synthetic measurements in figure 8. Vertical virtual brightnesses are shown in figure 10 left. As expected, a larger data scattering is observed compared to figure 6 and is due to the fact that the emissivity is not poloidally invariant. On the other hand, a separate, parabolic fit to data at $s < 0$ and $s > 0$ clearly shows that the center of the two parabolas does not occur at $s = 0$, but is shifted to the left and to the right in the two cases, respectively. This is remarkable as it already demonstrates that our method can recognise that the synthetic measurements in figure 8 are now associated to a profile that is qualitatively different from that of figure 5, although this difference

may not be apparent at a glance by comparing the input data for the two cases in figures 5 and 8. The separation of the emissivities by means of two shifted parabolas is even more clear after full inversion (figure 10).

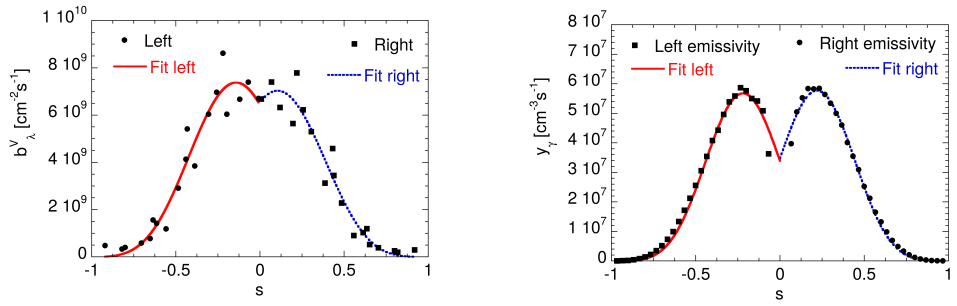

Figure 10. (left) Projection of the synthetic experimental brightness of figure 8 on a set of virtual vertical lines of sight for $s > 0$ and $s < 0$. Each projection is separately fitted with a parabolic function (solid and dashed lines). (right) Inverted emissivity profile obtained by applying equations 2.9 and 2.10 to each of the two fits of the left figure. The solid and dashed lines are a parabolic fit of the inverted emissivity for $s < 0$ and $s > 0$, respectively.

In more quantitative terms, we can compare w, y_0 and s_C for each of the two parabolas of the initial radial projection of the emissivities (figure 9) and of the inverted emissivities, with the results in table 2. In all cases, the inversion is capable to find the parameters of the radial projection of the emissivity with a discrepancy up to 25%, which is judged sufficient for analysis in between discharges and demonstrates the adequacy of the method even for the challenging case of non parabolic profiles produced by strong off-axis auxiliary heating.

Table 2. Comparison between inversion results and expected values for the width w, peak y_0 and centre s_C of the emissivity in case of the non parabolic profile of figure 9.

	Expected		Inversion results		Difference (%)	
	$s < 0$	$s > 0$	$s < 0$	$s > 0$	$s < 0$	$s > 0$
y_0 [cm^{-3}s^{-1}]	$5.79 \cdot 10^7$	$6.95 \cdot 10^7$	$5.68 \cdot 10^7$	$5.77 \cdot 10^7$	2	17
w	0.21	0.21	0.25	0.26	19	24
s_C	−0.24	0.29	−0.22	0.22	8	24

5 Conclusions

A generalised Abel inversion method has been developed to determine the emissivity profile starting from the sparse dataset of collimated brightness measurements along the 19 channels of the JET gamma-ray cameras. The aim of the method is to provide a quick and reliable way to determine the main parameters (peak value, width and centre) of the gamma-ray emissivity of JET plasmas in between discharges. The algorithm has been applied to synthetic brightness measurements originating from parabolic and non parabolic JET emissivity profiles and results of the inversion have been compared to the original input parameters. A typical noise level of 10% was assumed

in the synthetic measurements. In all cases, the algorithm is able to discriminate against parabolic and non parabolic profiles. In terms of profile parameters, we can determine the peak value, width and centre of the emissivity with an accuracy between 1 and 20% for parabolic and 2 to 25% for non parabolic profiles, respectively. The discrepancy is in general smaller for broader profile, when a larger fraction of the 19 camera channels provides non null measurements.
The results presented in this paper are primarily of relevance for the reconstruction of emissivity profiles from radiation measurements in high power tokamaks, but the method can also be applied to measurements along a sparse set of collimated lines of sight in general applications, provided that the surfaces at constant emissivity are known to have rotational simmetry.

Acknowledgments

This work has been carried out within the framework of the EUROfusion Consortium and has received funding from the Euratom research and training programme 2014-2018 under grant agreement No 633053. The views and opinions expressed herein do not necessarily reflect those of the European Commission.

References

[1] Kiptily V. et al., *gamma-ray diagnostics of energetic ions in JET*, *Nucl. Fusion* **42** (2002) pg. 999-1007

[2] Kiptily V.G., Cecil F.E. and Medley S.S., *Gamma ray diagnostics of high temperature magnetically confined fusion plasmas*, *Plasma Phys. Control. Fusion* **48** (2006) pg. R59-R82

[3] Tardocchi M., Nocente M. and Gorini G., *Diagnosis of physical parameters of fast particles in high power fusion plasmas with high resolution neutron and gamma-ray spectroscopy*, *Plasma Phys. Control. Fusion* **55** (2013) pg. 074014

[4] Chugunov I. et al., *Development of gamma-ray diagnostics for ITER*, *Nucl. Fusion* **51** (2011) 083010

[5] Nocente M. et al., *High resolution gamma-ray spectroscopy measurements of the fast ion energy distribution in JET* ^{4}*He plasmas*, *Nucl. Fusion* **52** (2012) pg. 063009

[6] Nocente M. et al., *Gamma-ray spectroscopy measurements of confined fast ions on ASDEX Upgrade*, *Nucl. Fusion* **52** (2012) pg. 094021

[7] Proverbio I. et al., *The* ^{12}C(^{3}He, pγ)^{14}N *reaction cross section for* γ*-ray spectroscopy simulation of fusion plasmas*, *Rev. Sci. Instrum.* **81** (2010) pg. 10D320

[8] Nocente M. et al., *Gamma-ray emission spectrum from thermonuclear fusion reactions without intrinsic broadening*, *Nucl. Fusion* **55** (2015) pg. 123009

[9] Tardocchi M et al., *Spectral broadening of characteristic* γ*-ray emission peaks from* ^{12}C(^{3}He, pγ)^{14}N *reactions in fusion plasmas*, *Phys. Rev. Letters* **107** (2011) pg. 205002

[10] Salewski M. et al., *Velocity-space observation regions of high-resolution two-step reaction gamma-ray spectroscopy*, *Nucl. Fusion* **55** (2015) 093029

[11] Giaz A. et al., *Characterization of large volume 3.5 " x 8 " LaBr*$_3$*:Ce detectors*, *Nucl. Instrum. Meth. A* **729** (2013) pg. 910-921

[12] Giaz A. et al., *Investigation on gamma-ray position sensitivity at 662 keV in a spectroscopic 3" x 3" $LaBr_3$:Ce scintillator*, *Nucl. Instrum. Meth. A* **772** (2015) pg. 103-111

[13] Nocente M. et al., *Energy resolution of gamma-ray spectroscopy of JET plasmas with a $LaBr_3$ scintillator detector and digital data acquisition*, *Rev. Sci. Instrum.* **81** (2010) 10D321

[14] Cazzaniga C. et al., *Response of $LaBr_3$(Ce) scintillators to 2.5 MeV fusion neutrons*, *Rev. Sci. Instrum.* **84** (2013) pg. 123505

[15] Cazzaniga C. et al., *Response of $LaBr_3$(Ce) scintillators to 14MeV fusion neutrons*, *Nucl. Instrum. Meth. A* **778** (2015) pg. 20-25

[16] Nocente M. et al., *High Resolution Gamma Ray Spectroscopy at MHz Counting Rates With $LaBr_3$ Scintillators for Fusion Plasma Applications IEEE Trans. Nucl. Sci.* **60** (2013) pg. 1408

[17] Nocente M. et al., *Experimental investigation of silicon photomultipliers as compact light readout systems for gamma-ray spectroscopy applications in fusion plasmas*, *Rev. Sci. Instrum.* **85** (2014) pg. 11E108

[18] Zychor I. et al., *High performance detectors for upgraded gamma ray diagnostics for JET DT campaigns*, submitted to *Physica Scripta* (2015)

[19] Abel N., *Journal fur die reine und angewandte Mathematik*, **1** (1826), pg. 153-157

[20] Eriksson J. et al., *Dual sightline measurements of MeV range deuterons with neutron and gamma-ray spectroscopy at JET*, *Nucl. Fusion* **55** (2015) pg. 123026

[21] Bonheure G. et al., *Neutron profiles and fuel ratio n_T/n_D measurements in JET ELMy H-mode plasmas with tritium puff*, *Nucl. Fusion* **46** (2006) pg. 725-740

[22] Craciunescu T. et al., *A comparison of four reconstruction methods for JET neutron and gamma tomography*, *Nuclear Instrum. Meth. A* **605** (2009) pg. 374-383

[23] Bielecki J. et al., *Phillips-Tikhonov regularization with a priori information for neutron emission tomographic reconstruction on Joint European Torus*, *Rev. Sci. Instrum.* **8** (2015) pg. 093505

[24] Wesson J. et al., *Tokamaks* (2004) Clarendon Press, Oxford

[25] Gorini G. et al., *Relationship between neutron yield rate of tokamak plasmas and spectrometer measured flux for different sight lines*, *Rev. Sci. Instrum.* **82** (2011) pg. 033507

[26] Yavorskij V. et al., *Confinement of fusion alpha particles in JET hollow current equilibrium*, *Nucl. Fusion* **43** (2003) pg. 1077

[27] Goloborod'ko V. et al., *Fokker-Planck 3-D modelling of axisymmetric collisional losses of fusion products in TFTR*, *Nucl. Fusion* **35** (1995) pg. 1523

[28] Nocente M. *Neutron and gamma-ray emission spectroscopy as fast ion diagnostics in fusion plasmas*, Ph.D. thesis (2012) available online at https://boa.unimib.it/handle/10281/28397